JACS
JOURNAL OF THE AMERICAN CHEMICAL SOCIETY

Article

Synthesis, Physical Properties, Multitemperature Crystal Structure, and 20 K Synchrotron X-ray Charge Density of a Magnetic Metal Organic Framework Structure, Mn(COH)(CHON)

Rasmus D. Poulsen, Anders Bentien, Marie Chevalier, and Bo B. Iversen

J. Am. Chem. Soc., **2005**, 127 (25), 9156-9166• DOI: 10.1021/ja051233z • Publication Date (Web): 03 June 2005

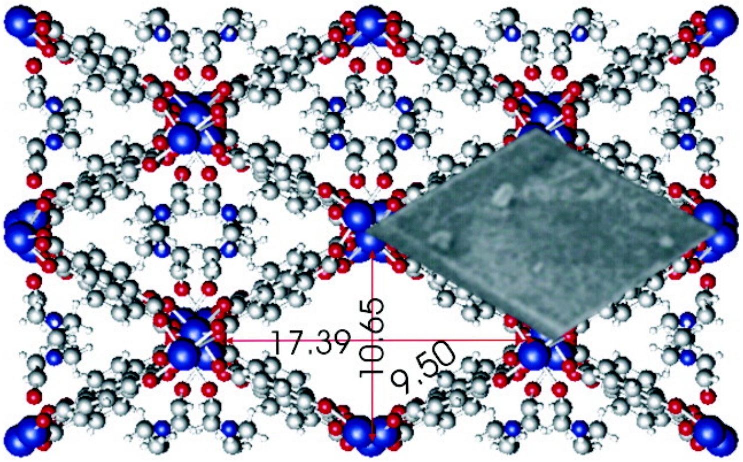

ACS Publications
High quality. High impact.

Journal of the American Chemical Society is published by the American Chemical Society. 1155 Sixteenth Street N.W., Washington, DC 20036

J|A|C|S
ARTICLES

Synthesis, Physical Properties, Multitemperature Crystal Structure, and 20 K Synchrotron X-ray Charge Density of a Magnetic Metal Organic Framework Structure, $Mn_3(C_8O_4H_4)_3(C_5H_{11}ON)_2$

Rasmus D. Poulsen, Anders Bentien, Marie Chevalier, and Bo B. Iversen*

Contribution from the Department of Chemistry, University of Aarhus, Langelandsgade 140, DK-8000 Aarhus, Denmark

Received March 8, 2005; E-mail: bo@chem.au.dk

Abstract: A new magnetic metal organic framework material has been synthesized, $Mn_3(C_8O_4H_4)_3(C_5H_{11}ON)_2$, **1**. Magnetic susceptibility measurements from 2 to 400 K reveal anti-ferromagnetic ordering at $\sim$4 K and a total magnetic moment of 6.0 μ_B. The magnetic phase transition is confirmed by heat capacity data (2−300 K). The crystal structure is studied by conventional single-crystal X-ray diffraction data at 300, 275, 250, 225, 200, 175, 150, 125, and 100 K, and synchrotron data at 20 K. There is a phase transition between 100 and 20 K due to ordering of the diethylformamide molecules. The X-ray charge density is determined based on multipole modeling of a second 20 K single-crystal synchrotron radiation data set. The electron distributions around the two unique Mn centers are different, and both have substantial anisotropy. Orbital population analysis reveals large electron donation (1.7 e) to each Mn atom and the maximum possible number of unpaired electrons is 3.2 for both Mn sites. Thus, there is a considerable orbital component to the magnetic moment. Bader topological analysis shows an absence of Mn−Mn bonding, and the magnetic ordering is via super-exchange through the oxygen bridges. Formal electron counting suggests Mn^{2+} sites, but this is not supported by the Bader atomic charges, Mn(1) = +0.11e, Mn(2) = +0.17e. The topological measures show the dominant metal−ligand interactions to be electrostatic, and a simple exponential correlation is derived between Mn−O bond lengths and the values of $\nabla^2\rho$ at the bond critical points.

Introduction

During the last couple of years there has been a strong revival of the field of coordination polymers and metal-organic framework (MOF) systems.[1] For gas storage applications, nanoporous systems based on Zn centers coordinated by dicarboxylate linkers have shown considerable promise.[2] By variation of the length of the carboxylate linker, incremental increases in cubic pore sizes over a large range have been achieved. One advantage of MOFs over zeolite materials is the larger chemical flexibility obtained by merging the coordination chemistry of transition metals with organic solid-state chemistry. The stereochemical control of the metal centers allows to some extent engineering of crystalline systems with specific structural configurations and properties,[1a] although it must be noted that for solvothermal synthesis methods the specific MOF structures depend quite strongly on process parameters (pressure, time, concentration, temperature). The presence of transition metals potentially allow for broader chemical reactivity than typically observed in zeolites, and the possibility for creating specific chemical functionality on the linker molecules is also very attractive.

We are focusing on MOFs with magnetic properties.[3] Magnetic MOFs may be considered as hybrids between classical 3D magnetic solids and molecular magnets.[4] The "LEGO" molecular building block approach in MOFs provides novel systems for studies of magnetic exchange mechanisms. Since the organic linker molecules can be incrementally increased in

---

(1) (a) Kitahawa, S.; Kitaura, R.; Noro, S. *Angew. Chem., Int. Ed.* **2004**, *43*, 2334−2375. (b) Lu, J. Y. *Coord. Chem. Rev.* **2003**, *246*, 327−347. (c) O'Keeffe, M.; Eddaoudi, M.; Li, H.; Reineke, T.; Yaghi, O. M. *J. Solid. State Chem.* **2000**, *152*, 1, 3−20. (d) Noro, S.; Kitura, R.; Kondo, M.; Kitagawa, S.; Ishii, T.; Matsuzaka, H.; Yamashita, M. *J. Am. Chem. Soc.* **2002**, *124*, 2568−2583. (e) Yaghi, O. M.; O'Keeffe, M.; Ockwig, N.; Chae, H. K.; Eddaoudi, M.; Kim, J. *Nature* **2003**, *423*, 705−714. (f) Li, H.; Eddaoudi, M.; O'Keeffe, M.; Yaghi, O. M. *Nature* **1999**, *402*, 276−279. (g) Chen, B. L.; Eddaoudi, M.; Hyde, S. T.; O'Keeffe, M.; Yaghi, O. M. *Science* **2001**, *291*, 1021−1023. (h) Yaghi, O. M.; Li, H.; Davis, C.; Richardson, D.; Groy, T. L. *Acc. Chem. Res.* **1998**, *31*, 474−484. (i) Eddaoudi, M.; Moler, D.; Li, H.; Reineke, T. M.; O'Keeffe, M.; Yaghi, O. M. *Acc. Chem. Res.* **2001**, *34*, 319−330. (j) Kubota, Y.; Takata, M.; Matsuda, R.; Kitaura, R.; Kitagawa, S.; Kato, K.; Sakata, M.; Kobayasho, T. C. *Angew. Chem., Int. Ed.* **2005**, *44*, 920−923.

(2) (a) Eddaoudi, M.; Kim, J.; Rosi, N.; Vodak, D.; Wachter, J.; O'Keeffe, M.; Yaghi, O. M. *Science* **2002**, *295*, 469−472. (b) Chae, H. K.; Siberio-Pérez, D. Y.; Kim, J.; Go, Y.; Eddaoudi, M.; Matzger, A. J.; O'keefe, M.; Yaghi, O. M. *Nature* **2004**, *427*, 523−527. (c) Hanson, K.; Calin, N.; Bugaris, D.; Scancela, M.; Sesov, S. C. *J. Am. Chem. Soc.* **2004**, *126*, 10502−10503. (d) Rosi, N.; Eddaoudi, M.; Vodak, D., Eckert, J.; O'Keeffe, M.; Yaghi, O. M. *Science* **2003**, *300*, 1127−1129. (e) Eddaoudi, M.; Li, H.; Yaghi, O. M. *J. Am. Chem. Soc.* **2000**, *122*, 1391−1397. (f) Rowsell, J.; Millward, A.; Park, K.; Yaghi, O. M. *J. Am. Chem. Soc.* **2004**, *126*, 5666−5667.

(3) (a) Miller, J. S.; Epstein, A. J. *Chem. Eng. News*. **1995**, *2*, 30−41. (b) Price, D. J.; Tripp, S.; Powell, A. K.; Wood, P. T. *Chem. Eur. J.* **2001**, *7*, 200−208. (c) Tynan, E.; Jensen, P.; Kelly, N. R.; Kruger, P. E.; Lees, A. C.; Moubaraki, B.; Murray, K. S. *Dalton Trans.* **2004**, 3440−3447.

(4) Kahn, O. *Molecular magnetism*; Wiley: New York, 1993.

10.1021/ja051233z CCC: $30.25 © 2005 American Chemical Society

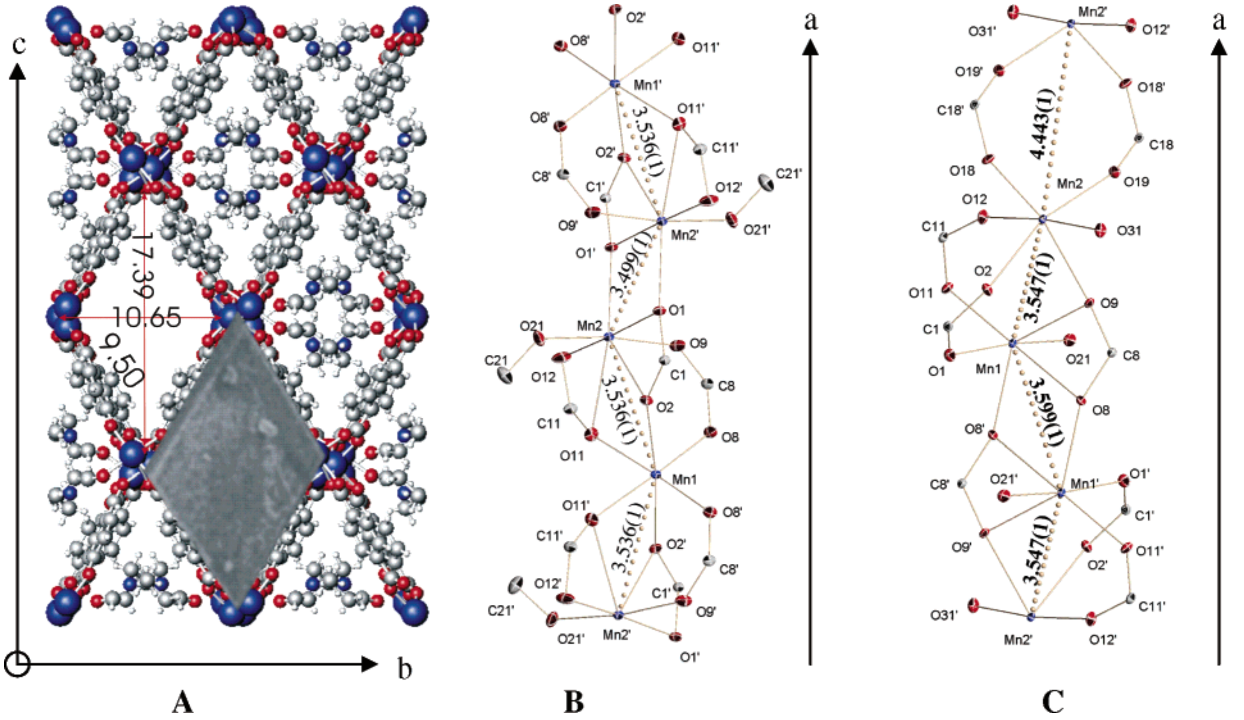

Figure 1. (a) View of the crystal structure along the *a*-axis. In one of the nanopores an electron microscope image of a single-crystal specimen is overlaid. Approximate pore dimensions are given in Å. (b) The main atoms in the Mn-chain showing the nomenclature and coordination environment of the metal centers. The Mn-chain runs approximately along the *a*-axis. (c) The Mn-chain in **2**. In both b and c the thermal ellipsoids are drawn at 50% level, and in all figures the axes directions are shown with arrows.

lengths as well as designed with specific electronic properties, it may be possible to fine-tune the magnetic superexchange pathways between the metal centers. Here we report the synthesis, magnetic properties, heat capacity, multitemperature crystal structure, and 20 K X-ray charge density of a new manganese-based MOF, $Mn_3(C_8O_4H_4)_3(C_5H_{11}ON)_2$, **1**, Figure 1. We have previously reported on the synthesis, physical property characterization, and synchrotron X-ray charge density of $Mn_2(C_8O_4H_4)_2(C_3H_7ON)_2$, **2**, where the diethylformamide (DEF) solvent of **1** is replaced with dimethylformamide (DMF).[5] The two structures are similar since they both contain chains of Mn atoms interconnected by carboxylate linkers, but they are not isostructural due to differences in the metal coordination. Nevertheless, the DMF-based structure, **2**, forms a good reference compound for **1**. In **2** no magnetic ordering is observed down to 2 K, and physical property data in combination with charge density analysis suggested that the metal atoms are high spin ions (Mn^{2+}) with five unpaired 3d electrons being the origin of the paramagnetic properties. As will be shown, this is in sharp contrast to the structure of **1**, which exhibits significant orbital contributions to the magnetism.

Contrary to many of the previously reported MOFs, solvent molecules do not occupy the nanoporous voids in either **1** or **2** but are coordinated directly to the magnetic Mn atoms creating crystalline systems with limited structural disorder. This makes it possible to experimentally determine their X-ray charge densities.[6] The structure of **1** consists of chains of manganese atoms aligned along the *a*-axis intraconnected by the carboxylate groups of the benzene-1,4-dicarboxylate (BDC) linker. This gives rise to one octahedral Mn(1) and one seven coordinated Mn(2) manganese site, Figure 1.

The X-ray charge density (CD) method has in recent years gone through an exciting revival due the availability of (i) area detectors for quick, reliable intensity recording, (ii) very high intensity, short wavelength, monochromatic synchrotron radiation to reduce systematic errors (extinction, absorption, anomalous scattering, no integration problems due to α_2 peak splitting), and (iii) development of stable helium cooling devices (increase resolution, improve thermal deconvolution, limit thermal diffuse scattering).[7] The present study provides an explicit demonstration of all these advances. Furthermore, CD studies in the past have often concerned well behaved, fully ordered crystal structures with relatively few (light) atoms. In **1** the DEF molecule maintains slight disorder even at 20 K, and the crystals are not strongly diffracting. Even so it is still possible with synchrotron radiation to determine a reliable CD. This illustrates that the experimental CD method today is a versatile tool, which is ready for application in main stream chemistry.

Experimental Section

Synthesis. The synthesis of the metal organic framework $Mn_3(C_8O_4H_4)_3(C_5H_{11}ON)_2$, **1**, is a *one-pot* reaction. A mixture of 0.166 g (1.0 mmol) of benzene 1,4-dicarboxylic acid (H_2BDC) and 5 mL of diethylformamide (DEF) was added to 0.287 g (1 mmol) $Mn(NO_3)_2\cdot 6H_2O$ dissolved in 2 mL of DEF. This was kept at 102 °C for 3 days. The crystals have the same shape as the monoclinic unit cell and are not resistant to extended exposure in air. Since the diffraction properties of the crystals are not as good as for **2**, numerous attempts (>30) were made to grow better quality crystals (variation of time, temperature,

---

[5] Poulsen, R. D.; Bentien, A.; Graber, T.; Iversen, B. B. *Acta Crystallogr. Sect. A* **2004**, *60*, 382−389.

[6] (a) Coppens, P. *X-ray Charge densities and chemical bonding*; Oxford University Press: Oxford, 1997. (b) Koritsanszky, T. S.; Coppens, P. *Chem. Rev.* **2001**, *101*, 1583−1628. (c) Coppens, P.; Iversen, B. B.; Larsen, F. K. *Coord. Chem. Rev.* **2005**, *249*, 179−195.

[7] Iversen, B. B.; Larsen, F. K.; Pinkerton, A. A.; Martin, A.; Darovsky, A.; Reynolds, P. A. *Acta Crystallogr. Sect. B* **1999**, *55*, 363−374.

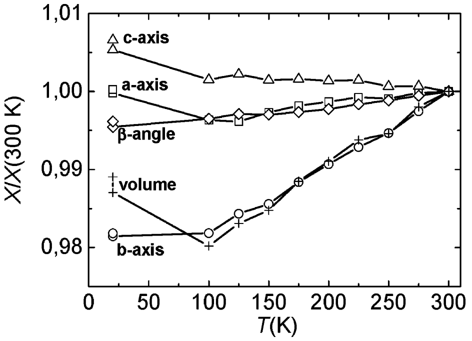

Figure 2. Unit cell parameters as a function of temperature relative to the 300 K values. Squares are the *a*-axis, circles the *b*-axis, triangles the *c*-axis, diamonds the β-angle, and crosses the unit cell volume.

concentrations). While our synthesis method is highly reproducible for preparation of **1**, we have not been able to grow strongly diffracting crystals for an "ideal" charge density study.

Physical Properties. The total heat capacity (C_p) and magnetic susceptibility (χ) was measured on a Quantum Design PPMS system at the Department of Chemistry, University of Aarhus, from 2 to 400 K on a pellet pressed from finely ground powder. Thermogravimetric analysis (TGA) and differential thermal analysis (DTA) were made from 25 °C to 570 °C using a Stanton-Redcroft TGA-DTA simultaneous thermal analyzer STA 1000/1500. A heating rate of 10 °C/min was applied in an Ar gas flow. The crystal structure of **1** is thermally stable up to about 500 K, where a complicated decomposition pattern initiates (see Supporting Information).

Multitemperature Single-Crystal X-ray Diffraction. At conventional laboratory X-ray sources the crystals we have obtained of **1** are not diffracting significantly above $\sin\theta/\lambda = 0.8$ Å^{-1}, and this makes detailed electron density modeling problematic. Furthermore, an initial room-temperature crystal structure investigation revealed that the DEF molecule coordinated to the Mn(2) site is disordered over (at least) two sites. To examine this disorder, and the thermal properties of the crystal structure in general, we collected conventional Mo Kα crystal structure data sets at 300, 275, 250, 225, 200, 175, 150, 125, and 100 K. The data were collected on a different crystal specimen than the 20 K synchrotron charge density data described below. Furthermore, to confirm the phase transition between 100 and 20 K a second synchrotron data set was collected at 20 K on a third crystal. Data reduction and structure solution was done with the Bruker SMART suite of programs (SAINT+, SADABS, SHELX),[8] and full experimental details and crystallographic data are reported in the Supporting Information.

In Figure 2 the temperature dependence of the unit cell parameters is plotted, and between 100 and 20 K there is an abrupt change. The 20 K data point is confirmed by separate measurements on two different crystals during different beam time periods. As discussed below, the heat capacity shows a significant change of slope between 100 and 20 K in support of a phase transition. The thermal expansion of the crystal above 100 K is found to be anisotropic with the major expansion occurring along the *b*-axis, which is perpendicular to the Mn-chain (see Figure 1). The expansion is in the direction of the disordered DEF molecule and into the cavity. As the framework structure expands, the DEF molecule has less spatial restraints, and this eventually leads to the disorder and the phase transition.

Figure 3 shows key atomic displacement parameters (ADPs) as a function of temperature. The disorder is clearly seen in the ADPs of the N(21) and C(22) atoms of the DEF moiety, which are much larger than for the carboxylate ligands. In other words the ADPs model the disorder of the DEF molecule. For the O(21) and C(21) atoms the disorder is less pronounced because the different orientations of the DEF molecules almost superimpose for these atoms. Figure 3 supports the presence of a phase transition between 100 and 20 K, where the curvatures of the ADP curves suddenly change from concave to convex and the ADP have a sudden decrease. The occupancy of the second site of the disordered DEF molecule is smoothly decreasing with temperature from 17.5% at room temperature to 9% at 100K, but at 20 K the occupancy of the second site is too low for reliable modeling. Thus, the phase transition observed in the unit cell parameters and the heat capacity is due to freezing out of the DEF disorder. Indeed at 20 K the O(21) and C(21) atoms have ADPs, which are comparable to the values obtained for the other atoms. It is noteworthy that the ADP plots of all atoms, i.e., not just the DEF molecule, change curvature between 100 and 20 K. This supports that the structure in fact goes through a subtle phase transition. If the disorder simply froze out on the DEF site, then it may be expected that only these ADPs show a sudden decrease.

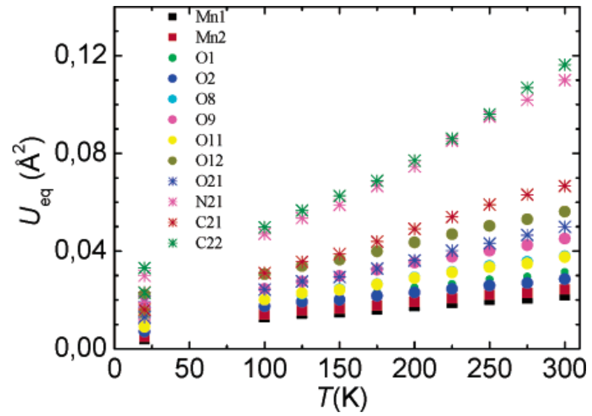

Figure 3. Atomic displacement parameters (U_{eq}) as a function of temperature. Squares correspond to Mn atoms, circles to oxygen ligands, and stars to atoms in the DEF molecule.

Synchrotron X-Ray Diffraction for Charge Density. Synchrotron radiation data ($\lambda = 0.394$ Å) were collected at beam line X3A1 at the National Synchrotron Light Source. A single crystal (0.0875 × 0.075 × 0.080 mm^3) mounted on a few carbon fibers was placed in the cold He stream of a Pinkerton type cooling device[9] fitted on a Huber type 512 four-circle diffractometer. The diffracted radiation in the ϕ-scan experiment was detected with a Bruker 6000 CCD detector mounted on the 2θ arm of the diffractometer at a distance of 4.7 cm. The data extend to a maximum $\sin\theta/\lambda$ of 1.26 Å^{-1}, but in general the high order data are fairly weak. Use of a much larger crystal is not possible since this creates problems with centring of the crystal in the narrow spatial plateau of the synchrotron beam. A second smaller data set was measured at 20 K on another crystal of lesser quality during a separate beam time period. Details of the data are enclosed in the Supporting Information. The data reduction and structure solution was performed with the Bruker SMART package (SAINT+, SADABS, SHELX)[8] although data averaging was done with program SORTAV.[10] The weakness of the high order data is directly revealed in the much increased internal *R*-factors at low *d*-values, see Table 1. To avoid the influence of spurious single-measurement outliers, we have only retained reflections measured three times or more in the final data set.[7] An empirical absorption correction was performed based on the considerable redundancy of the data.[8] Some hydrogen atoms were located by Fourier synthesis, while the remaining H atoms were placed on calculated positions. The electron density was modeled with the Hansen−Coppens multipole model[11] using the program XD.[12] The multipole model used $l_{\max} = 4$ for Mn, $l_{\max} = 3$ for C, N, and O, and

---

(8) Sheldrick, G. S. SAINT+, SADABS and SHELXL programs included in the Bruker SMART CCD software, 2003.

(9) Hanson, B. L.; Martin, A.; Harp, J. M.; Bunick, C. G.; Parrish, D. A.; Kirschbaum, K.; Bunick, G. J.; Pinkerton, A. A. *J. Appl. Crystallogr.* **1999**, *32*, 814−820.

(10) Blessing, R. H. *J. Appl. Crystallogr.* **1997**, *30*, 421−426 and references therein.

(11) Hansen, N. K.; Coppens, P. *Acta Crystallogr. Sect. A* **1978,** *34*, 909−921.

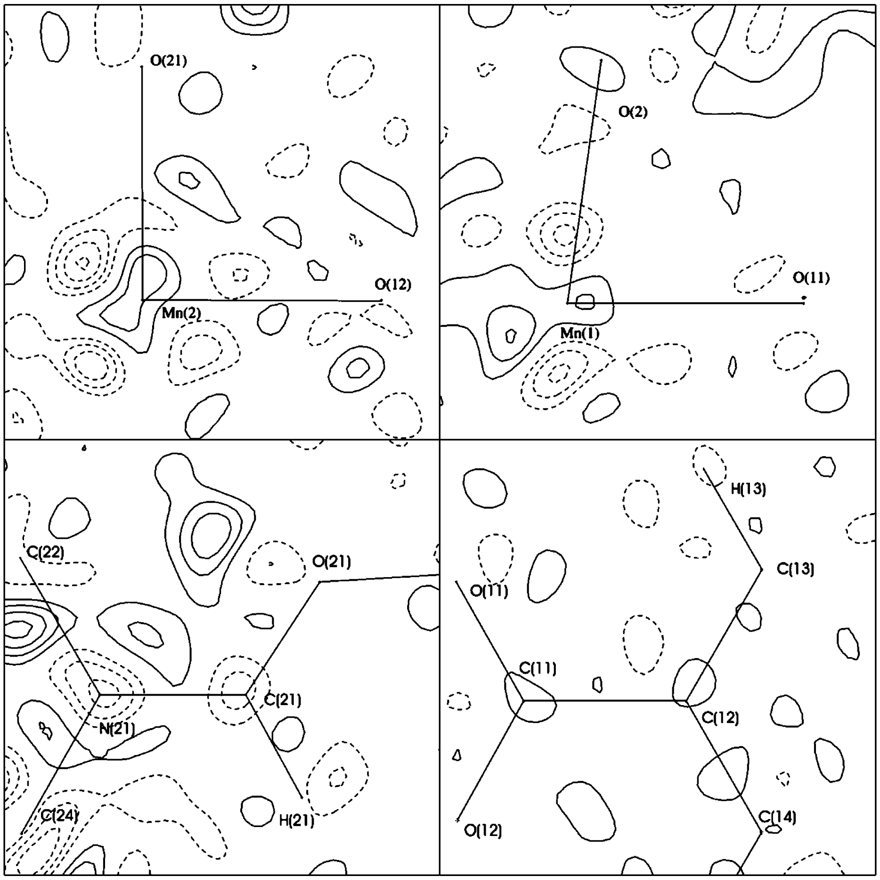

Figure 4. Residual density in (a) the O(21)−Mn(2)-O(12) plane, (b) the O(2)−Mn(1)-O(11) plane, (c) the O(21)−C(21)-N(21) plane, (d) a representative BDC plane C(11)−C(12)-C(13). The contour level is 0.1 e/Å^3 with solid contours being positive and negative dashed. The resolution is 0.8 Å^{-1}.

one monopole and one bond directed dipole on H. For the non-hydrogen atoms, single Slater type radial functions were employed, whereas the hydrogen atoms used the SDS scattering factor.[13] Ionic scattering factors[14] were employed for Mn^{2+}. The hydrogens were moved along the refined bond directions to positions giving bond distances equal to average neutron diffraction values. Free refinement of the κ' and κ'' radial expansion/contraction parameters on some of the atoms presented a challenge. For the Mn sites, the κ'' parameters diverged when corefined with the atomic displacements parameters (ADP). We therefore fixed the Mn positions and ADPs at values obtained from a high order refinement ($\sin\theta/\lambda > 0.8$ Å^{-1}). We have not been able to model the small features observed in the residual density about 0.5 Å from the Mn(2) center, Figure 4.

Use of anharmonic parameters or more flexible radial functions (e.g. separate κ parameters for each multipole order) do not significantly influence these residual features. To probe the origin of the difficulties, multipole refinements were carried out with successive removal of shells of the high order data. When refining only data with $\sin\theta/\lambda < 0.9$ Å^{-1}, all parameters can be corefined, yet the final electron density parameter values are similar to the values obtained with the full data set (in particular the κ parameters on Mn). In the residual density the hole near Mn(2) decreases from 0.4 e/Å^3 to 0.2 e/Å^3, even though the same data are used in the Fourier summation of the residual density ($\sin\theta/\lambda < 0.8$ Å^{-1}). The main difference between the two refinements is in the modeling of the ADPs. We have compared the topological measures at the bond critical points in the two models (all data versus $\sin\theta/\lambda < 0.9$ Å^{-1}). The results are similar but, for example, the values in the C−C bonds are slightly higher (ρ, $\nabla^2\rho$) with the full data set and in better agreement with literature values. So although the high order data are not of excellent quality, we retain all data in the modeling

Table 1. Crystallographic and Experimental Details

formula,	$Mn_3O_{14}N_2C_{34}H_{34}$
weight	859.45
crystal color	clear light colorless
space group	$I2/a$ (No. 15),
T (K)	20(1)
a (Å)	19.108(4)
b (Å)	10.653(2)
c (Å)	17.391(3)
β (°)	94.17(3)
V (Å^3)	3530.5(4)
λ (Å)	0.394
Z	4
ρ_{calcd} (g cm^{-3})	1.617
μ (mm^{-1})	0.190
T_{max}/T_{min}	1.00/0.98
integrated reflections	198090
unique reflections	27526 (all), 21225 ($N_{measured} > 2$)
R_{int} ($d > 1$ Å), N_{terms}, N_{means}	0.0391, 24320, 1837
R_{int} ($d > 0.75$ Å), N_{terms}, N_{means}	0.0461, 46427, 4354
R_{int} ($d > 0.5$ Å), N_{terms}, N_{means}	0.0706, 119714, 14742
R_{int} (all), N_{terms}, N_{means}	0.0918, 181387, 27089
$\sin(\theta)/\lambda_{max}$ (Å^{-1})	1.26
N_{par}	648
N_{obs} (2σ-cutoff)	12388
$R(F)$, $R(F^2)$	0.0648, 0.0646
$R_w(F)$, $R_w(F^2)$	0.0389, 0.0740
goodness of fit	0.632

---

(12) Koritsanszky, T.; Howard, S. T.; Richter, T.; Macchi, P.; Volkov, A.; Gatti, C.; Mallinson, P. R.; Farrugia, L. J.; Su, Z.; Hansen, N. K. *XD − A Computer Program Package for Multipole Refinement and Topological Analysis of Charge Densities from Diffraction Data*, 2003. URL: http//xd.chem.buffalo.edu.

(13) Stewart, R. F.; Davidson, E. R.; Simpson, W. T. *J. Chem. Phys.* **1965**, *42*, 3175−3187.

(14) Clementi, E.; Roetti, C. *Atomic Data Nucl. Data Tables* **1974**, *14*, 177.

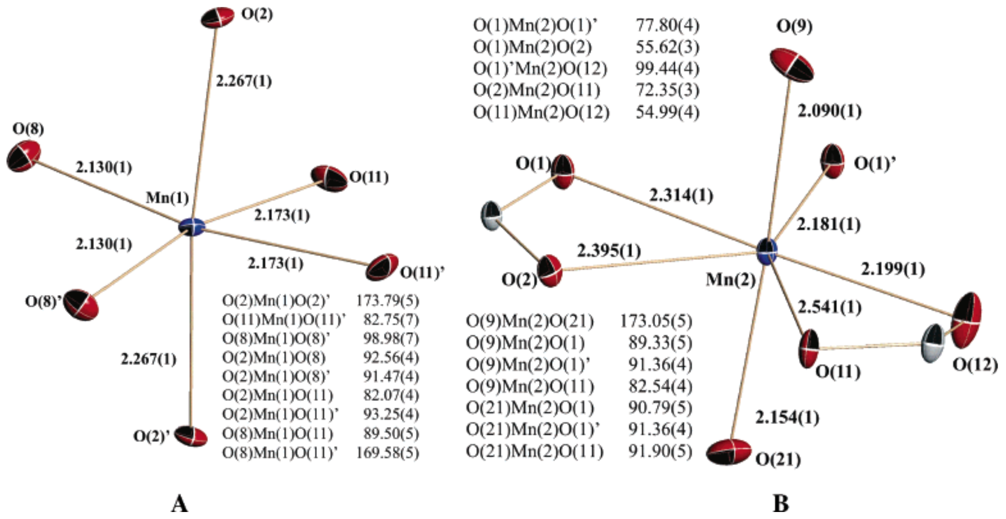

Figure 5. The coordination environment around the two metal sites. Bond length are given in Å and angles in degrees. The thermal ellipsoids are drawn at the 50% level.

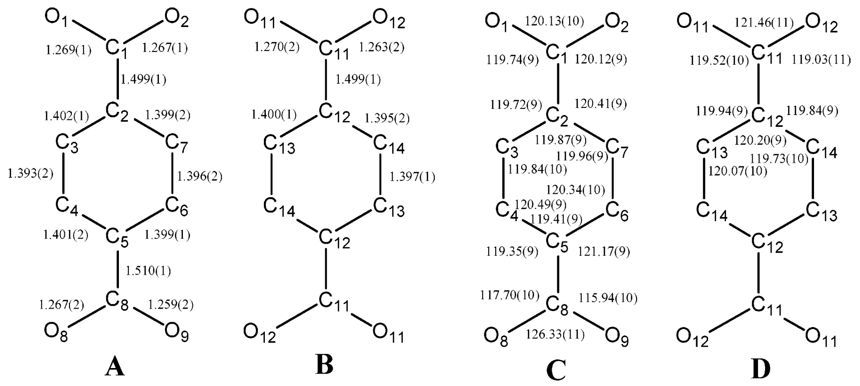

Figure 6. Geometry of the linker molecules. A and B shows the bond lengths (Å), C and D the bond angles (deg).

and accept the higher residual factors in the fit. It is also unclear what the exact cut-off level in sin θ/λ should be to improve the modeling situation.

For the DEF solvent molecule coordinated to Mn(2) the κ refinement was also difficult. In the residual density, features of around 0.3−0.4 e/Å^3 are observed in the solvent region away from the bonds, Figure 4c. These features presumably are due to slight disorder remaining even at 20 K, but the occupancy of the other site(s) is too small to be modeled (< few %). Nevertheless, the disorder makes refinement of the solvent molecule κ' and κ'' parameters problematic, and they were fixed to unity. In the final model the following kappa parameters were refined: two common κ parameters were introduced on the Mn sites in the form of one monopole $\kappa' = 1.103(6)$ and one multipole $\kappa'' = 1.41(3)$. For all non-DEF and non-H atoms the two standard κ' and κ'' parameters were refined for each chemically unique atom type ($\kappa'(\mathrm{O}) = 0.990(3)$, $\kappa''(\mathrm{O}) = 0.91(4)$, $\kappa'(\mathrm{C_{carboxylate}}) = 1.057(11)$, $\kappa''(\mathrm{C_{carboxylate}}) = 0.94(4)$, $\kappa'(\mathrm{C_{benzene}}) = 1.070(5)$ and $\kappa''(\mathrm{C_{benzene}}) = 0.631(15)$). The Hirshfelds rigid bond test[15] gives a mean $\Delta_{\mathrm{A-B}}$ value of 11 pm^2, and only Mn(2) has a high value of 18 pm^2. Plots of the residual density in other regions of the structure show no significant features (see Supporting Information). Further details of the data collection and data reduction are listed in Table 1.

Results and Discussion

Structure. In Figure 1 the structure is shown at 20 K based on modeling of synchrotron X-ray diffraction data. The inner part of the voids are occupied by the DEF solvent molecules, which are bound at one coordination site to Mn(2). The structure consists of rows of carboxylate-bridged Mn atoms interconnected by the benzene dicarboxylate linkers. Thus, there appears to be a unique magnetic direction along the Mn chains (*a*-axis), with much larger interchain distances (> 9.50 Å) than intrachain distances (3.536(1) Å for Mn(1)−Mn(2) and 3.499(1) Å for Mn(2)−Mn(2′)). The Mn(1) atom has a slightly distorted octahedral coordination, Figure 5, and it is placed on a rotation axis. Mn(2) has a coordination number of seven with an axis formed by O(9) and O(21). In the basal plane perpendicular to the O(9)−Mn(2)-O(21) axis O(1)′, O(2) and O(12) are close to having a trigonal geometry. However, the O(1) and O(11) atoms bisect the angles and form a distorted pentagonal bypyramidal coordination due to the "locked" carboxylate structure. The seven-coordinate geometry is well-known for lanthanides, but unusual for 3D transition metals.

Formal electron counting provides additional insight about the coordination. All the carboxylate groups are delocalized, Figure 6, which means that each oxygen formally carries a $-{}^1/_2$e charge. A carboxylate oxygen shared between metal atoms will therefore count as $-{}^1/_4$e. Both Mn atom then have formal charges of +2e, and this gives a combined +6e charge for the three metal atoms in agreement with the stoichiometry of the structure. From a structural point of view it may be argued that Mn(2)−O(11) is too long to be a bond, and if this bond is

---

(15) (a) Harel, M.; Hirshfeld, F. L. *Acta Crystallogr. Sect. B* **1974**, *31*, 162−172. (b) Hirshfeld, F. L. *Acta Crystallogr. Sect. A* **1976**, *32*, 239−244.

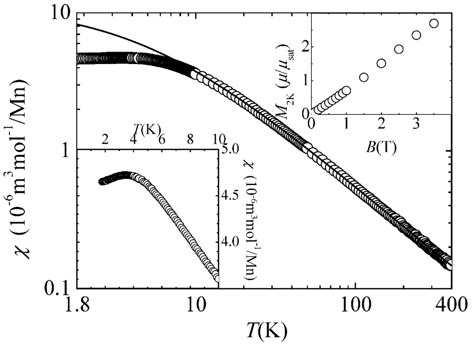

Figure 7. Magnetic susceptibility (χ) as function of temperature (T) measured in a magnetic field (B) of 0.1 T. The black solid line is a Curie−Weiss modeling of $\chi(T)$ above 25 K. The lower left inset shows the same data on linear scale in the low-temperature region. The upper right inset shows the magnetization (M) as function of B measured at 2 K.

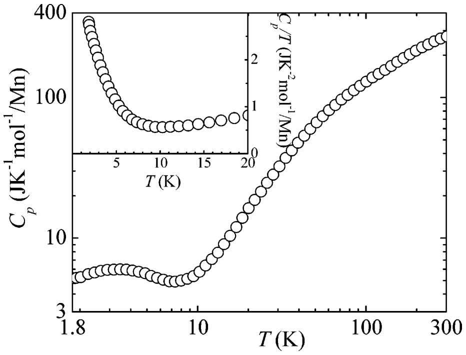

Figure 8. Specific heat (C_p) as function of temperature (T). The inset shows the same data plotted for C_p/T as function of T.

omitted the formal charges are +2.5e on Mn(1) and +1.75e on Mn(2). The topological analysis of the experimental charge density discussed below reveals a bond critical point for Mn(2)−O(11) in support of the expected +2 formal charge assignment. If the Mn2−O(11) bond is lacking Mn(2) is octahedrally coordinated with the O(2) atom being locked in a nonideal coordination by the geometric restraints of the carboxylate group, Figure 5.

Physical Properties. In Figure 7 we show the magnetic susceptibility (χ) measured between 2 and 400 K in a magnetic field of 0.1 T. At $T > 25$ K a fit with the Curie−Weiss law ($\chi = C/(T - \Theta) + \chi_0$, where $C = N\mu_0\mu_B^2\mu_{eff}^2/(3k_B)$, N is the density of magnetic ions in the relevant units, μ_{eff} is the effective moment, Θ is the Weiss temperature, and χ_0 is a temperature independent term) gives $\Theta = -5$ K, $\mu_{eff} = 6.0\ \mu_B$, and $\chi_0 = 7.6 \cdot 10^{-9}$ m^3/mol. μ_{eff} is relatively close to the theoretical value of 5.9 μ_B for a free Mn^{2+} ion.[16] The lower left inset of Figure 7 is a replot of the low-temperature region of χ(T) and shows that χ(T) has a maximum at approximately 4 K. This taken together with the negative Weiss temperature ($\Theta = -5$ K) and a linear magnetization with magnetic field (upper right inset in Figure 7) is an indication of an antiferromagnetic ordering of the Mn ions below approximately 4− 5 K.

This interpretation is supported by measurements of the specific heat (C_p) as function of temperature which can be seen in Figure 8. A broad peak is observed below 10 K with a peak maximum at approximately 3.5 K. Below 10 K the phonon contribution to C_p is still significant and since there exists no nonmagnetic reference compound it is difficult to calculate the entropy change in the magnetic transition. However, from the inset of Figure 8, which shows C_p/T as function of T, we estimate the entropy change ($\Delta S = \int(\Delta C/T)dT$) to range from approximately 5 J K^{-1} mol^{-1}/Mn to 15 J K^{-1} mol^{-1}/Mn. This is in reasonable agreement with what can be expected from a magnetic ordering of high spin Mn^{2+} ions, with $J = 5/2$ and $\Delta S = R \ln(2J + 1) = 14.9$ J K^{-1} mol^{-1}. The substantial entropy change during the phase transition shows that it is a bulk effect of the material. At approximately 100 K there is a change in the slope of the curve. This is related to the freezing out of the solvent disorder as discussed above.

The magnetic susceptibility is a macroscopic property, which does not reveal the detailed electronic origin of the magnetism in the structure. Thus, no distinction is made between the two structurally different Mn sites, nor is covalence in the bonding considered which can limit the validity of the approximation that the magnetic moments are localized on the Mn sites only. In the structure of **2** the microscopic picture obtained from the synchrotron X-ray charge density revealed both the Mn sites to be high spin Mn^{2+} ions with close to single electron occupancy in the five 3d orbitals. This was in excellent agreement with the magnetic moment of 5.9 μ_B estimated from magnetic susceptibility data. Furthermore, **2** was shown to be paramagnetic even at 2 K. As will be shown the origin of the magnetism is different in **1** even though the total magnetic moment is almost identical to that of **2**.

Charge Density. In Figures 9 and 10 we show plots of the static deformation density and the Laplacian distribution ($\nabla^2\rho$) in two planes containing the metal atoms. A selection of plots is deposited with the Supporting Information including plots of the linker and solvent molecules, which show expected features. The static deformation density is obtained as the difference between the density of the refined multipole model and that of a promolecule (superposition of free spherical atoms placed at their unit cell positions). The Laplacian distribution is widely used in CD analysis to depict regions of charge concentration and charge depletion.[17] There are very clear nonspherical features around both the metal centers, and the maps of Figures 9 and 10 show that these features are represented in similar ways in the static deformation and Laplacian distributions. Deformation densities are sometimes criticized for being arbitrary constructs,[17] whereas the Laplacian has a direct physical meaning. Here the information about electron density deformation is present in both maps. The fact that the electron distributions of both Mn atoms are far from spherical is a direct experimental demonstration that the simple picture of a high spin Mn^{2+} ion is inadequate. Furthermore, the density features are different at the two Mn sites showing that the macroscopic magnetic susceptibility is a result of a complex microscopic electronic structure.

From the refined multipole populations we can derive experimental 3d orbital populations on the metal sites, Table 2.[18] Due to the site symmetry of Mn(1) we must place the z-axis of the local coordinate system (LCS) along the crystal b-axis direction during refinement. However, using the program ERD we have subsequently calculated the Mn(1) d-orbital populations

---

(16) Ashcroft, N. W.; Mermin, N. D. *Solid State Physics*; CBS Asia Publishing: 1976.

(17) Bader, R. F. W. *Atoms in molecules. A quantum theory*; Clarendon Press: Oxford, 1990.

(18) Holladay, A.; Leung, P.; Coppens, P. *Acta Crystallogr. Sect. A* **1983**, *39*, 377−387.

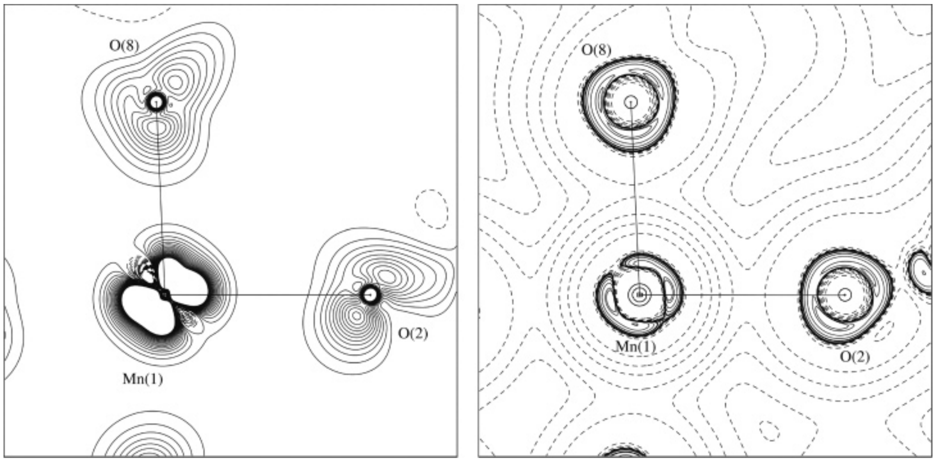

Figure 9. Static deformation (a) and Laplacian (b) maps in the O(2)−Mn(1)−O(8). Contour level is 0.1 e/Å^3 for the deformation map, where solid lines are positive contours and dashed lines are negative. For the Laplacian map the contour level is $2^x \times 10^y$ ($x = 0, 1, 2, 3$ and $y = -2, -1, 0, 1, 2, 3$) for the positive dashed contours and $2^x \times 10^y$ ($x = 1,2,3$ and $y = -2, -1, 0, 1, 2, 3$) for the solid negative contours.

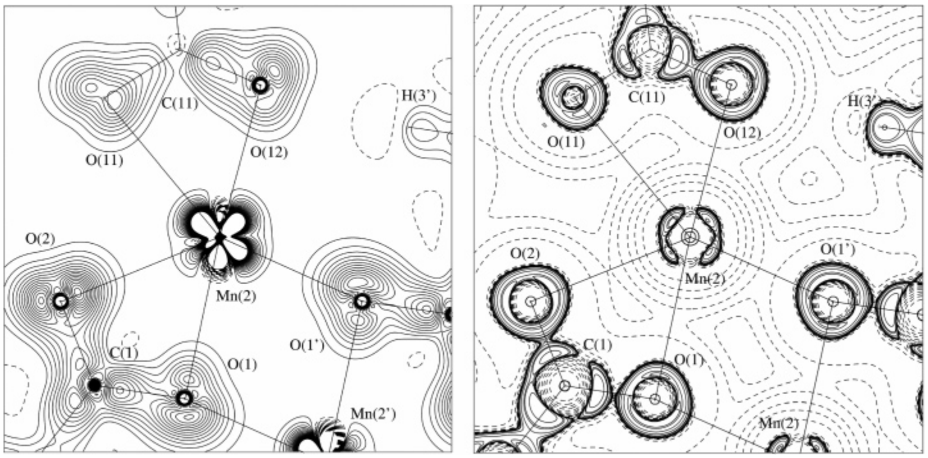

Figure 10. Static deformation and Laplacian maps in the Mn(2)−O(1)−O(1′)−O(2)−O(12) plane. O(11) is bend slightly out of plane. Contour level as in Figure 9.

Table 2. 3d-Orbital Population Derived from the Refined Multipole Coefficients[a]

	d_{z^2}	$d_{x^2-y^2}$	d_{xz}	d_{yz}	d_{xy}	total
Mn(1)	1.63(5)	1.41(5)	0.98(5)	1.09(5)	1.68(5)	6.79
	24%	21%	14%	16%	25%	
	0.37	0.59	0.98	0.91	0.32	3.2
Mn(1)	1.04(5)	1.37(5)	1.57(5)	1.49(5)	1.32(5)	6.79
	15%	20%	23%	22%	20%	
	0.96	0.63	0.43	0.51	0.68	3.2
Mn(2)	1.08(5)	0.96(5)	1.78(5)	1.50(5)	1.41(5)	6.73
	16%	14%	27%	22%	21%	
	0.92	0.96	0.22	0.50	0.59	3.2
Mn(2)	1.96(5)	1.19(5)	0.86(5)	1.48(5)	1.24(5)	6.73
	29%	18%	13%	22%	18%	
	0.04	0.81	0.86	0.52	0.76	3.2

[a] For each entry the second line gives relative populations in % and the third line the maximum number of unpaired electrons. Estimated standard deviations on the electron populations are given in parentheses. For each metal atom the first entry refers to structure based LCS (see text), while the second entry is for the LCS that minimizes orbital cross terms.

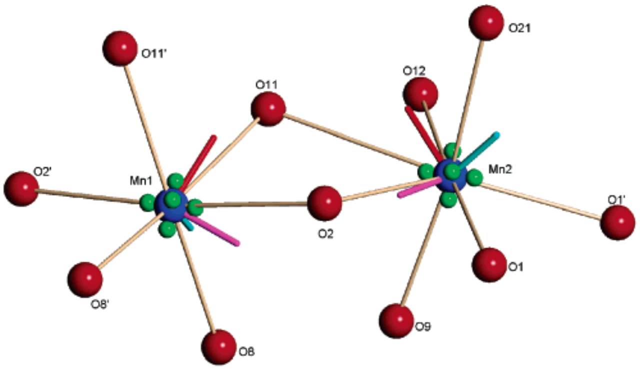

Figure 11. Local coordinate systems obtained by minimization of orbital cross terms.[19] Red is the *x*-axis, purple the *y*-axis and turquiose the *z*-axis. Green spheres are the (3, −3) points of the negative Laplacian distribution (valence shell charge concentrations) of the Mn atoms. The (3, −3) points are drawn to scale at exact positions, and they are not located along particular axes.

with the *z*-axis pointing toward O(2) and the *x*-axis toward O(11).[19] For Mn(2) we have chosen the *z*-axis toward O(21) and the *x*-axis toward O(1). While axes definitions are straightforward in high-symmetry coordination environments, the choice of LCS is not clear in low symmetry environments. Sabino and Coppens have argued that a consistent choice of LCS could be the one that minimizes the orbital cross terms.[19] This choice of LCS is plotted in Figure 11 and corresponding populations are also listed in Table 2.

A total electron donation from the ligands of 1.79e relative to the free ion is observed for Mn(1) and of 1.73e for Mn(2). The "natural" LCS minimizing cross terms does not have a

---

(19) Coppens, P.; Sabino, J. *Acta Crystallogr. Sect. A* **2003**, *59*, 127−131.

Table 3. Selected Bond Distances and Topological Measures at Bond Critical Points[a]

bond	distance	R_{ij}	d_1	ρ	$\nabla^2\rho$	G	V	H	G/ρ	VS
Mn(1)−O(2)	2.267(1)	2.267	1.136	0.22	5.2	0.31	−0.25	0.06	1.42	d−c
Mn(1)−O(8)	2.130(1)	2.130	1.059	0.36	8.4	0.54	−0.48	0.05	1.51	c−d
Mn(1)−O(11)	2.173(1)	2.173	1.082	0.31	7.4	0.46	−0.40	0.06	1.50	c−d
Mn(2)−O(1)	2.314(1)	2.315	1.144	0.20	4.8	0.28	−0.23	0.05	1.37	c−d
Mn(2)−O(2)	2.395(1)	2.395	1.166	0.18	4.2	0.24	−0.19	0.05	1.36	c−d
Mn(2)−O(9)	2.090(1)	2.091	1.059	0.36	8.7	0.55	−0.49	0.06	1.54	c−c
Mn(2)−O(11)	2.541(1)	2.560	1.249	0.12	2.7	0.15	−0.11	0.04	1.27	d−c
Mn(2)−O(12)	2.199(1)	2.199	1.101	0.27	6.5	0.39	−0.33	0.06	1.47	c−c
Mn(2)−O(21)	2.154(1)	2.155	1.065	0.33	8.2	0.51	−0.45	0.06	1.53	c−d
Mn(2)−O(1)′	2.181(1)	2.181	1.083	0.30	7.2	0.44	−0.38	0.06	1.47	c−d

[a] R_{ij} (Å) is the sum of distances between the critical point and the atomic attractors, d_1 is the distance (Å) from the first atom to the critical point, ρ is the electron density (e/Å^3), and $\nabla^2\rho$ is the Laplacian (e/Å^5). G, V, and H are the kinetic energy density, the potential energy density, and the total energy density respectively (hartree Å^{-3}). The random errors estimated from the least squares procedure are typically on the third decimal for ρ and $\nabla^2\rho$. This is much smaller (order of magnitude) than the systematic error due to the specific choice of density model. Therefore, we only list the values to the second decimal in ρ and first decimal in $\nabla^2\rho$. The last column lists qualitative features of the valence shell (VS) Laplacian in the bond directions. The critical points in the valence shell Laplacian are not located in the directions of the chemical bonds (see Figure 11), and "concentration" and "depletion" only points out that the bond direction lies in a region with highly negative or highly positive Laplacian values (see Figures 15 and 16). In the last column the first entry is for the first atom and second entry for the second atom, c = concentration, d = depletion.

straightforward interpretation with respect to the chemical bonds. However, no matter what choice of LCS both the Mn sites must be considered high-spin with large populations in all orbitals. In Table 2 we also list the maximum possible number of unpaired electrons on the metal sites. For both sites this is about 3.2 electrons, which is 1.8 electron short of the value derived from the magnetic susceptibility. This means that the magnetic moment has a large orbital component as is also evident from the anisotropy of the d-orbital populations. However, some of the moment may in fact also be located on the ligands.

In Table 3 we list different topological measures of the metal−ligand bond critical points (bcp), while bcps for all other bonds are listed in the Supporting Information. We also locate a weak metal−metal bcp between Mn(2) and Mn(2′), but not between Mn(1) and Mn(2). However, when examining the eigenvalues at the Mn(2)−Mn(2′) bcp it is seen that λ_2 has an abnormal low value close to zero, and the critical point in reality is probably a ring critical point. This is supported by examination of the Laplacian in the Mn(2)−O(1)−Mn(2)′ plane, Figure 10. The contour map shows a minimum in the plane as expected for a ring critical point, although the map is very flat in the Mn(2)−Mn(2)′ direction. Thus, there is not direct Mn−Mn bonding and the magnetic ordering presumably is due to super-exchange. For the coordination bonds we obtain expected values of ρ_{bcp} between 0.11 and 0.36 e/Å^3, and positive values of the Laplacian. In all the Mn−O bonds the total energy density is positive and G/ρ is fairly large.[20] The topological measures therefore indicate that all metal−ligand interactions are predominantly of the closed shell type. Nevertheless, it is the subtle orbital interactions between the metals and the bridging oxygens that appear to be responsible for the magnetic ordering. It is interesting that the bond to the solvent molecule, Mn(2)−O(21), is quite short with a relatively high ρ_{bcp}. Thus, there is no indication that this coordination site lends itself to substitution.[21] To obtain a chemically active metal site inside a nanoporous MOF probably will take a structure with weaker metal−ligand bonds.

In Figure 12 the Laplacian values at the bcps are plotted against the Mn−O bond lengths. The plot also contains the values obtained for **2**[5] as well as literature values from a charge density study of a trinuclear iron complexes with carboxylate ligands.[22] The values of $\nabla^2\rho$ have an exponential decrease with increasing values of the metal−oxygen bond length, and the fit indeed is very good. An exponential relation is also observed for closed shell hydrogen bonds where shorter bonds have larger values of $\nabla^2\rho$.[23] For hydrogen bonds there is a transition region when going from closed shell hydrogen bonds with positive $\nabla^2\rho$ values to very short covalent hydrogen bonds with negative $\nabla^2\rho$ values. Such compression of the bonds is not reached for the metal-carboxylate interactions even though some of the Fe−O distances in the plot actually are quite short. Formally, the Mn^{2+} ions of **1** and **2** and the Fe^{3+} ions involved in the very short M−O bonds in Figure 12 have the same electron configuration but differ in nuclear charge. Following the arguments made for hydrogen bonds, the strong single-exponential correlation for a large range of M−O bonds is a fingerprint of the close shell nature of these bonds.

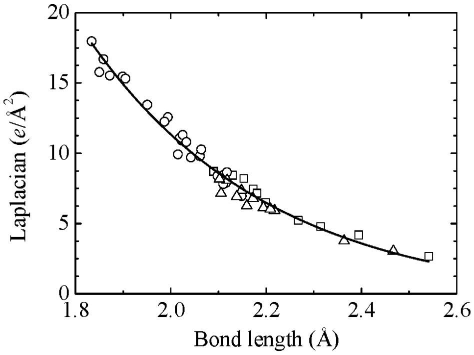

Figure 12. $\nabla^2\rho$ as a function of metal−O$_{carboxylate}$ bond length. Squares are from the present study of **1**, triangles from the study of **2**[5] and circles refer to Fe−O bonds in a series of trinuclear carboxylates.[22] The fit to a single-exponential function gives $y = 2235 \times \exp(-x/0.38) - 0.61$ (R = 0.98).

The differences between the two Mn atoms can be further probed by calculating various atomic properties as defined by the zero flux boundary condition in the quantum theory of atoms in molecules,[17] Table 4. The atomic charges of Mn(1) and Mn(2)

---

(20) Macchi, P.; Sironi, A. *Coord. Chem. Rev.* **2003**, *238*, 383−412.

(21) Macchi, P.; Schultz, A. J.; Larsen, F. K.; Iversen, B. B. *J. Phys. Chem. A.* **2001**, *105*, 9231−9242.

(22) Overgaard, J.; Larsen, F. K.; Schiøtt, B.; Iversen, B. B. *J. Am. Chem Soc.* **2003**, *125*, 11088−11099.

(23) (a) Espinosa, E.; Lecomte, C.; Molins, E. *Chem. Phys. Lett.* **1999**, *300*, 745−748, (b) Espinosa, E.; Alkorta, I.; Elguero, J.; Molins, E. *J. Chem. Phys.* **2002**, *117*, 5529−5542.

Table 4. Atomic Properties as Defined within the Quantum Theory of Atoms in Molecules[a]

1	charge (e)	TBV (Å^3)	BV2 (Å^3)	dipole moment (Debye)	**2**	charge (e)	TBV (Å^3)	BV2 (Å^3)	dipole moment (Debye)
Mn(1)	+0.11	68.0	67.1	0.03	Mn(1)	+2.04	69.2	68.6	0.09
Mn(2)	+0.17	66.7	66.1	0.22	Mn(2)	+2.03	68.1	67.5	0.03
O(1)	−1.37	116.3	87.4	0.16	O(1)	−1.15	111.9	100.0	0.59
O(2)	−1.38	98.5	87.2	0.17	O(2)	−1.24	111.3	101.4	0.65
O(8)	−1.24	117.2	86.1	0.30	O(8)	−1.13	99.5	94.1	0.54
O(9)	−1.31	121.3	86.8	0.34	O(9)	−1.17	100.6	95.8	0.64
O(11)	−1.55	106.0	87.2	0.16	O(11)	−1.25	108.2	100.5	0.57
O(12)	−1.38	128.9	87.1	0.52	O(12)	−1.20	117.7	102.7	0.68
					O(18)	−1.25	120.7	105.4	0.64
					O(19)	−1.26	120.1	104.1	0.61
O(21)	−1.47	139.5	93.8	0.57	O(21)	−1.30	121.4	106.5	0.60
					O(31)	−1.45	122.5	105.5	0.66
C(1)	+ 0.78	53.1	37.9	0.77	C(1)	+1.90	29.5	28.1	0.87
C(2)	+0.15	70.0	44.6	0.11	C(2)	−0.28	77.1	68.8	0.06
C(3)	+0.17	67.9	48.2	0.11	C(3)	−0.03	74.7	73.1	0.33
C(4)	+0.19	68.8	49.7	0.25	C(4)	−0.12	85.1	76.5	0.53
C(5)	+0.19	62.1	43.1	0.18	C(5)	−0.07	83.4	68.3	0.35
C(6)	+0.20	85.2	50.0	0.20	C(6)	−0.19	85.2	76.9	0.36
C(7)	+0.17	76.2	50.1	0.21	C(7)	−0.31	103.5	78.7	0.57
C(8)	+0.96	45.1	34.9	0.68	C(8)	+1.76	40.3	33.4	0.98
C(11)	+0.79	62.3	37.0	0.53	C(11)	+1.78	37.1	32.7	0.87
C(12)	−0.07	68.0	47.4	0.34	C(12)	−0.38	87.8	70.4	0.06
C(13)	+0.23	65.9	50.7	0.45	C(13)	−0.19	97.1	78.4	0.35
C(14)	+0.39	60.6	42.0	0.55	C(14)	−0.36	94.7	78.3	0.46
					C(15)	−0.02	76.3	65.2	0.18
					C(16)	−0.09	84.1	77.5	0.32
					C(17)	−0.36	96.7	80.6	0.37
					C(18)	+0.191	33.3	31.7	0.84

[a] The two entries are for $Mn_3(C_8O_4H_4)_3(C_5H_{11}ON)_2$, **1**, and for $Mn_2(C_8O_4H_4)_2(C_3H_7ON)_2$, **2**. TBV is the total basin volume, whereas BV2 is the volume of the portion of the basin in which the electron density is equal to or exceeds 0.002 au.

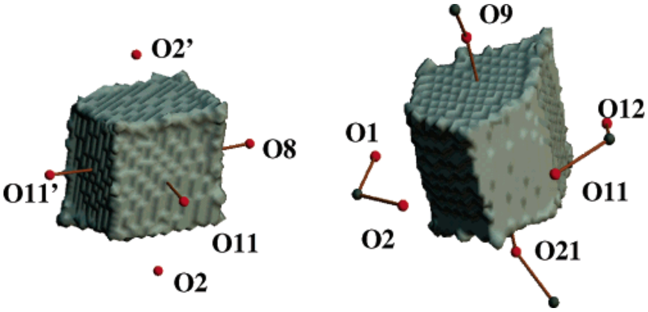

Figure 13. Atomic surfaces of the two Mn atoms determined from the zero flux condition on the experimental charge density. Mn(1) is to the left, and Mn(2), to the right.

are low and quite similar (+0.17 and +0.11, respectively), and this disagrees strongly with the formal charge assignment of Mn^{2+} ions. The measured charges also contradict the mixed valence picture suggested by the formal electron count on the structure with the Mn(2)−O(11) omitted. Even though the atomic charges are similar, there are significant differences in the metal charge distributions as seen for example in the atomic dipole moments. Mn(1) has a small dipole moment in correspondence with the high-symmetry coordination, whereas Mn(2) has a significant moment reflecting the asymmetric coordination. The differences in the shapes of the two Mn charge distributions are visualized in Figure 13.

In Table 4 we also list the atomic properties obtained in the synchrotron charge density study of **2**.[5] The most striking difference is as mentioned above the different Mn atomic charges. While the structure of **1** has almost neutral Mn atoms, **2** has the “expected” ionic charges. Even so, the atomic volumes of the Mn atoms are very similar in the two structures. This means that the tightness of the Mn charge distributions must be larger in **1**, and the electron donation into the 3d orbitals is spatially located inside the atom away from the atomic surfaces. This corresponds to a picture of the 3d orbitals being quite-contracted in space, yet still involved in bonding. The differences in the radial distributions of the Mn valence electrons are reflected in the kappa expansion/contraction parameters, which are larger than unity in **1** ($\kappa' = 1.1$, $\kappa'' = 1.4$) but smaller than unity in **2** ($\kappa' = 0.96$, $\kappa'' = 0.7$). The oxygen ligands of **1** have quite similar atomic charges (−1.24e to −1.55e), but a relatively larger spread in the atomic dipole moments (0.16 to 0.57 Debye). The atomic volumes range from 98.5 Å^3 for O(2) to 139.5 Å^3 for O(21) of the DEF molecule. There appears to be little correlation between the atomic volumes of the oxygen atoms and their atomic charges. For **1** it seems that the oxygen atoms bridging two metal atoms (O(1), O(2), O(11)) have smaller dipole moments than the oxygen atoms with single metal coordination, but this is not reproduced in **2** (O(8) and O(9) bridging). The lack of correlation suggests that the distributions of charge inside the atomic volumes have considerable variation even among structurally similar carboxylate atoms. As shown in Figure 6, the C−O bond lengths fall in a narrow range (1.259(2) Å to 1.270(2) Å), which from a structural point of view would indicate electron delocalization and great similarity between the carboxylate oxygen atoms. Table 4 reveals that the oxygen atoms of **1** are more concentrated than in **2** (smaller volume, same charge). In correspondence with this the oxygen dipole moments are greater in **2** than in **1**.

There is another striking difference between **1** and **2** besides the Mn charge distributions. In **1** the benzene carbon atoms are slightly positive, while in **2** they are slightly negative (Table 4). This change of polarity, and the larger atomic charges of **2** in general, has consequences for the electrostatic potential in the nanopores. In Figure 14 the electrostatic potential is shown

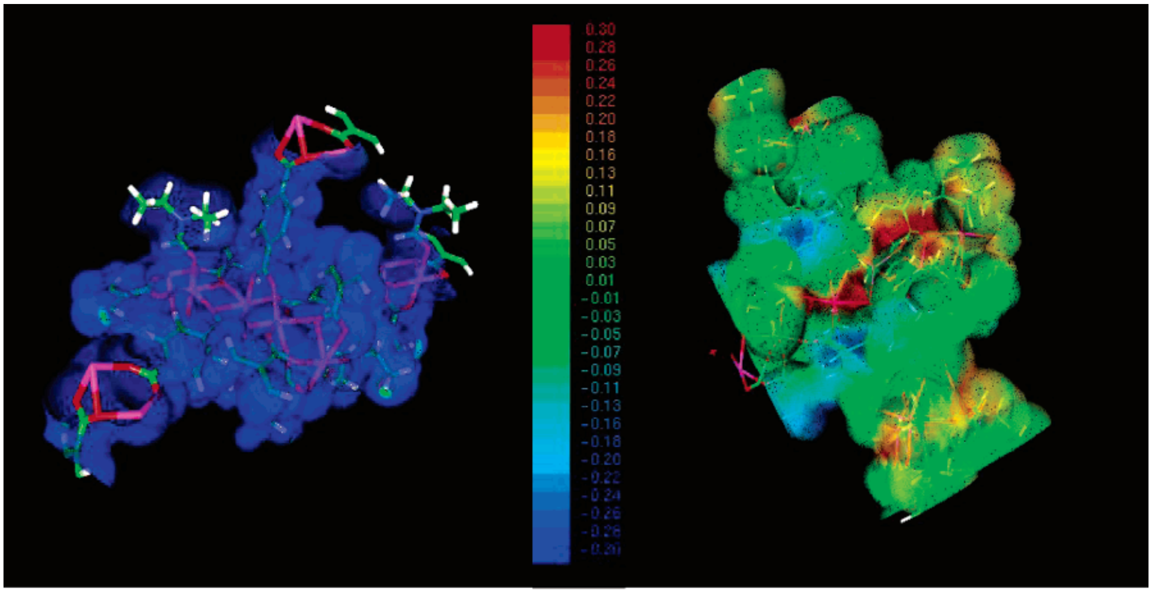

1 **2**

Figure 14. The electrostatic potentials of **1** and **2** calculated from the experimental electron density and plotted on density isosurfaces of 0.01 e/Å^3. The potential ranges from −0.3 e/Å (blue) to 0.3 e/Å (red).

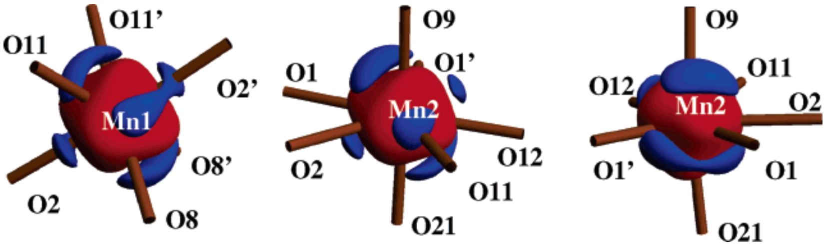

Figure 15. Isosurface plots of the valence shell Laplacian distributions of the two Mn atoms of **1**. The Mn(2) atom is shown in two different orientations. Red is the regions of minimal $\nabla^2\rho$ (charge concentrations, $\nabla^2\rho < -1300$ e/Å^5), and blue the regions of maximum $\nabla^2\rho$ (charge depletions, $\nabla^2\rho > 1000$ e/Å^5).

in parts of the pores of **1** and **2** drawn with the same color coding. The potential of **1** is much more uniform than that of **2**, which has both negative and positive regions. MOF structures have been intensively studied with regard to gas storage.^{2} Presumably neutral gas molecules such as molecular hydrogen are bonded to the walls of the framework by weak dispersion forces, and these increase in strength with increasing electron density. It is not straightforward to predict from the potential where neutral molecules will be energetically favored, but it is a worthy future study to examine if any correlations can be made with measured gas storage abilities.

An important question is why **1** has more covalence in the metal−ligand bonds than **2**. It is the orbital interactions between the metals and the bridging oxygens which presumably are responsible for the super-exchange mechanism that leads to magnetic ordering in **1** but not in **2**. The major structural difference along the Mn-chain is that in **1** all Mn atoms are bridged by oxygen atoms, whereas in **2** there is a very long bridge of 4.4525(2) Å based on a whole carboxylate unit (Figure 1).

Even though the electron density contains no spin information. it is still interesting to probe empirically if it contains some kind of signature related to the magnetic interactions. Unpaired electrons located in a specific orbital may give rise to valence shell concentrations. In Figures 15 and 16, isosurface plots of the valence shell concentrations and depletions of the Mn atoms in **1** and **2** are shown. Corresponding plots for the oxygens atoms are included in the Supporting Information.

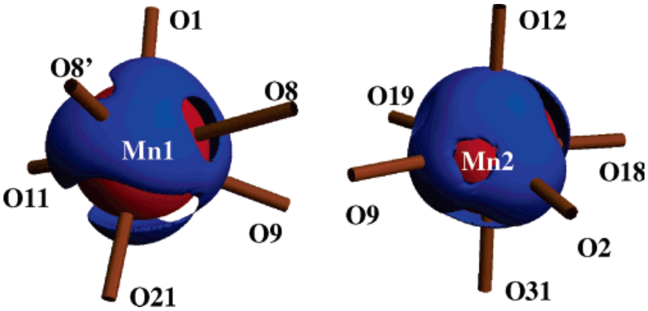

Figure 16. Isosurface plots of the valence shell Laplacian distributions of the two Mn atoms of **2**. Red is the regions of minimal $\nabla^2\rho$ (charge concentrations, $\nabla^2\rho < -500$ e/Å^5), and blue the regions of maximum $\nabla^2\rho$ (charge depletions, $\nabla^2\rho > 700$ e/Å^5).

The large differences in 3d-orbital populations between **1** and **2** are indirectly seen in Figures 15 and 16, where the Mn atoms of **2** have almost homogeneous charge depletions in the outer shell (spherical Mn^{2+} ions), while those of **1** show a complex topology. When examining the chemical bond directions along the Mn−O−Mn chain of **1** a picture of alternating charge depletions and concentrations is observed, Figure 17. Whether this systematic topology of the valence shells is related to the magnetism we do not know, but it will be interesting to examine this further in related MOF structures.

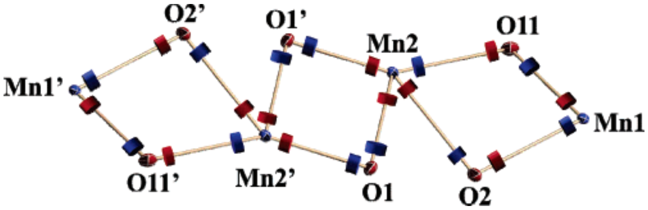

Figure 17. Schematic representation of the valence shell charge concentrations (red) and depletions (blue) along the Mn−O−Mn chain of **1**.

Conclusion

The present study has documented an antiferromagnetic ordering in a new metal organic framework compound. The information obtained from macroscopic physical properties (heat capacity, magnetic susceptibility) was supplemented by analysis of the electron density at a “subatomic” level. The experimental electron density was determined from multipole modeling of 20 K synchrotron X-ray diffraction data. Bader topological analysis gives no evidence for direct metal−metal chemical interaction, corroborating that the magnetic ordering takes place via super-exchange. The super-exchange presumably is via the bridging oxygen atoms, and the lack of magnetic ordering in **2** can be explained by one Mn−Mn linkage being an entire carboxylate group. Orbital population analysis reveals large electron donation from the ligands to the metals, and the measured magnetic moment must have considerable orbital components. The electron donation is quantified in the Bader atomic charges, which show almost neutral Mn atoms but with quite different atomic basins for the unique Mn sites. This reiterates that a microscopic charge density view is desirable as a complement to macroscopic property measurements on magnetic materials.

Acknowledgment. We gratefully acknowledge the beam time obtained at beam line X3A1, the National Synchrotron Light Source, Brookhaven National Laboratory. The SUNY X3 beam line at NSLS was supported by the Division of Basic Energy Sciences of the US Department of Energy (DEFG0286ER45231). The work was supported the DANSYNC center under the Danish Research Councils. We are indebted to the Carlsberg Foundation and the Danish Research Councils for funding a Quantum Design PPMS. We thank Dr. Jacob Overgaard for fruitful discussions and help with plotting the electrostatic potential.

Supporting Information Available: Thermal analysis (TGA/DTA), crystallographic information files (CIF) for all measured data (including multipole coefficients for the 20 K data), maps of the residual density, the static deformation density and the Laplacian of the electron density, Laplacian isosurface maps for Mn and oxygen atoms. This material is available free of charge via the Internet at http://pubs.acs.org.

JA051233Z